

Wetting by biomolecular condensates increases membrane lipid packing and dehydration

Agustín Mangiarotti¹, Macarena Siri¹, Ziliang Zhao^{1,2}, Leonel Malacrida^{3,4}, Rumiana Dimova¹

¹ Max Planck Institute of Colloids and Interfaces, Science Park Golm, 14476 Potsdam, Germany.

² Current address: Leibniz Institute of Photonic Technology e.V., Albert-Einstein-Straße 9, 07745 Jena, Germany; and Institute of Applied Optics and Biophysics, Friedrich-Schiller-University Jena, Max-Wien Platz 1, 07743 Jena, Germany

³ Departamento de Fisiopatología, Hospital de Clínicas, Facultad de Medicina, Universidad de la República, Montevideo, Uruguay.

⁴ Advanced Bioimaging Unit, Institut Pasteur of Montevideo and Universidad de la República, Montevideo, Uruguay.

Address correspondence to: Rumiana.Dimova@mpikg.mpg.de, lmalacrida@pasteur.edu.uy, agustin.mangiarotti@mpikg.mpg.de

Abstract

Membrane wetting by biomolecular condensates recently emerged as a critical phenomenon in cell biology, involved in a great diversity of processes across different organisms. However, understanding the molecular mechanism behind this process is still missing. Exploiting ACDAN and LAURDAN properties as nano-environmental sensors in combination with phasor analysis of hyperspectral and lifetime imaging microscopy, we obtained vital information on the process of condensate formation and membrane wetting. The results reveal that glycinin condensates display differences in water dynamics when changing the salinity of the medium as a consequence of rearrangements in the secondary structure of the protein. The analysis of membrane-condensates interaction indicated a correlation between increased wetting affinity and enhanced lipid packing, demonstrated by a decrease in water dipolar relaxation at both protein and polymer systems. These results suggest a general mechanism to tune membrane order by condensate wetting.

Introduction

Biomolecular condensates play a crucial role in cellular organization and metabolism¹. These dynamic assemblies arise by liquid-liquid phase separation and are involved in a broad range of cell processes, from genomic organization^{2, 3}, to stress responses^{4, 5}, and virus infection⁶, to name a few. More recently, the interaction of these membraneless-organelles with membrane-bound compartments has emerged as a new means for intracellular compartmentation, protein assembly, and signaling^{7, 8}. Among others, membrane-biomolecular condensates interactions are involved in developing tight junctions⁹, the formation of the autophagosome¹⁰, the signal transduction in T cells¹¹, the assembling of virus capsid proteins¹², and in the biogenesis and fission of droplets in the endoplasmic reticulum¹³. Recently, membranes have been reported to control the size of intracellular condensates and modify their material properties¹⁴. Furthermore, the crosstalk between membranes and condensates can promote phase separation coupling in the lipid and the protein phases^{15, 16}, ¹⁷ also shown in cytoplasm mimicking systems¹⁸. In this manner, membrane-condensate interactions have become an emerging and exciting field, but important cues are still missing towards understanding the underlying mechanisms of the resulting structural changes and remodeling. Given the small size of condensates, quantifications of these interactions are often precluded *in-vivo*¹⁹. Thus, important insight about the material properties of condensates have been obtained *in-vitro*, taking advantage of their relatively easily reconstitution²⁰.

Membrane wetting by condensates was first reported more than a decade ago for giant unilamellar vesicles (GUVs) enclosing an aqueous two-phase system (ATPS)^{18, 21}. The ATPS formed from solutions of poly(ethylene glycol) (PEG) and dextran is probably the best understood example. The PEG-dextran ATPS constitutes a convenient model of the crowded cytoplasm to study liquid-liquid phase separation in contact with membranes^{22, 23, 24}. These pioneering studies revealed that membrane wetting by condensates can give rise to several biologically relevant processes of membrane remodeling such as inward and outward budding, nanotubes formation, and fission of membrane compartments²². GUV tubulation was also observed when condensate protein species are bound to the membrane via NTA-lipids²⁵. Recently, we addressed the interaction between non-anchored protein condensates and membranes, describing a landscape of the morphological changes driven by this interaction and providing a theoretical framework that allows quantifying it²⁶. In addition, we reported the phenomenon of mutual remodeling of the interface between the condensate and the membranes, named interfacial ruffling²⁶. These present the first steps in understanding the interaction between membranes and condensates at the micron-scale. However, the molecular mechanism governing it is far from being known and to our knowledge not yet explored. Here, we provide an experimental framework to unravel the governing forces at the molecular scale by employing a comprehensive set of techniques. Hyperspectral imaging and

fluorescence lifetime imaging microscopy (FLIM) was combined with the phasor plot analysis, whereby we exploited the sensitivity of two nano-environmental sensitive probes, 6-acetyl-2-dimethylaminonaphthalene (ACDAN), and 6-dodecanoyl-2-dimethylaminonaphthalene (LAURDAN). In this way, we characterize water dynamics changes in the protein condensates at increasing salt concentration, their interaction with membranes and the associated environmental changes at molecular level, both in the membrane and the condensate. For characterizing the changes in the protein condensates, we employed attenuated total reflectance - Fourier-transform infrared spectroscopy (ATR-FTIR) and Raman microscopy and obtain a molecular view on the protein structural changes taking place during phase separation. Our results show that proteins undergo structural changes inside the condensates when modifying the salt concentration in the medium, leading to different confined water properties. These changes are exhibited by altered water dynamics which is sensed by ACDAN^{27, 28, 29}, providing a means for analyzing physico-chemical changes in the condensates nano-environment.

We also investigated the molecular origin of the different degrees of membrane wetting (wetting affinity) by the condensates when changing the solution salinity²⁶. We show that with increasing wetting affinity, the membrane in contact with the condensates becomes dehydrated and more packed than the bare membrane. Taken together, the results obtained with protein condensates and with ATPS systems point to a general phenomenon for the membrane-condensate interaction, taking a step further in understanding the molecular basis underlying this interaction.

Results

Hyperspectral Imaging of ACDAN senses crowding and water dynamics in condensate nano-environment

The di-methylaminonaphtalene probes (DAN) are a family of polarity-sensitive dyes, the spectral changes of which respond to the solvent dipolar relaxation^{30,31} (see Fig. 1a). Because intracellular water is the most abundant dipolar active molecule in biological systems, DAN probes can be employed as sensors for changes in water dynamics intracellular lumen^{31, 32, 33} and in membranes^{31, 34}. As shown in Fig. 1b, when the DAN fluorescent probes are excited, there is an increase in the dipolar moment of the dye. If the solvent molecules are free to reorient and align with the dye dipole, the emission spectrum of the probe is red-shifted as a consequence of the energy reduction due to solvent relaxation (Fig. 1b,c). Conversely, in an environment where the dynamics of the solvent molecules is precluded, and water cannot reorient around the dye at the excited state, the spectrum falls towards the blue region. One of the probes we employ is ACDAN, which is a water-soluble dye that has been previously used to characterize the aqueous environment in yeast^{28, 32}, HeLa cells³³, and most recently for the study of *in-vivo* macromolecular crowding of zebra fish lenses²⁷. Here, we exploit the sensitivity of ACDAN by using hyperspectral imaging combined with the phasor plot analysis²⁷, to probe the nanoenvironment in biomolecular condensates formed by glycinin. Glycinin is one of the most abundant storage proteins in the soybean. It forms homogeneous solutions in water at different concentrations, but undergoes self-coacervation in the presence of sodium chloride^{35, 36}. Hyperspectral imaging produces a stack of images, in which each pixel contains spectral information, as schematized in Fig. 1d. Fourier transform of the spectral data from each pixel allows building a 2-dimensional scatter plot with the real and imaginary components (G and S) as axes of the phasor space, see inset in Fig. 1e and Methods. Here, the angular dependence carries information about the center of mass of the emission spectra in all pixels, while the spectra broadening is reflected in the radial dependence of the data. Figure 1e shows the spectral phasor plot of glycinin in water at different concentrations. While in water, ACDAN has an emission spectrum centered at 520 nm, when increasing the protein-water ratio the spectrum is blue shifted reflecting the associated reduction of dipolar relaxation. ACDAN spectroscopic properties provide an accurate quantitative readout of the water activity (confinement) and, in consequence, protein-water ratio and crowding²⁷. An easy way of visualizing the spectral shifts consists of extracting the histogram for the pixel distribution along a trajectory defined by the data, i.e. two-cursor analysis, see Methods. Figure 1f shows the histograms of the data at different glycinin concentrations as shown superimposed in Fig. 1e. The x-axis describes the changes in the water dipolar relaxation, which decreases when increasing the protein concentration. For a quantitative and statistical analysis, the center of mass of these histograms, which reflects the degree of dipolar relaxation, can be calculated

(see Methods) and plotted as exemplified in Fig. 1g. The use of phasor plot for analysing ACDAN fluorescence is fundamental since it avoids biases by assuming *a priori* a model for data interpretation^{27, 37}. On the other hand, phasor plot properties such as linear combination and reciprocity principle enable quantitatively addressing the problems under study.

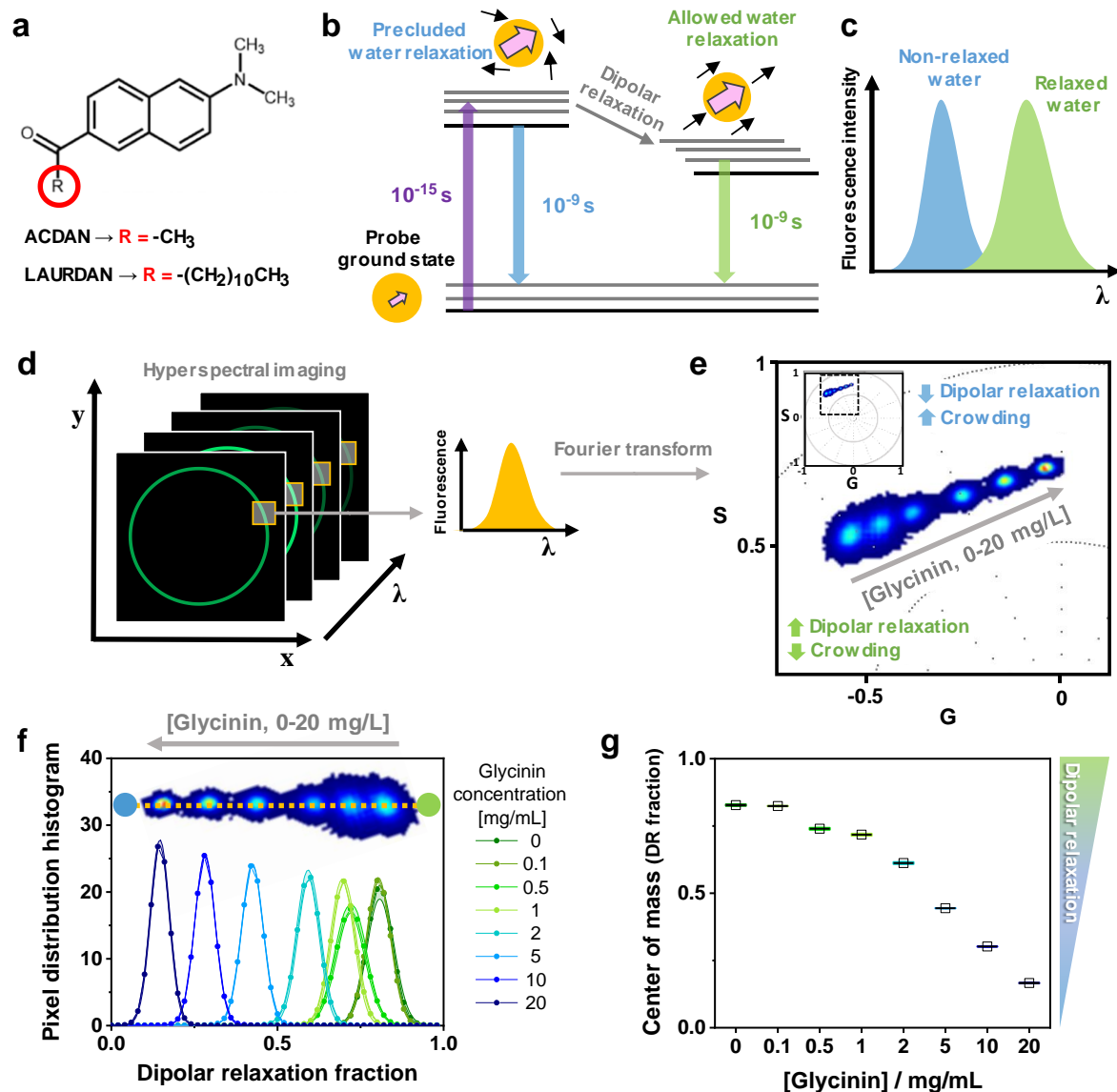


Figure 1. DAN probes solvatochromism allows the quantification of water dipolar relaxation and crowding.
a. Molecular structure of the DAN probes, highlighting the differences between ACDAN (water soluble) and LAURDAN (partitions in membranes). **b.** Perrin-Jablonski diagram illustrating the phenomenon of solvent dipolar relaxation. When the solvent dipoles (black arrows) are free to align with the probe during its excited-state (probe dipole is presented with pink arrow), the dipole energy is reduced and the fluorescence emission is red-shifted, as exemplified in **c**. **d.** Hyperspectral imaging consists of acquiring images at different emission wavelengths to generate a lambda-stack. Each pixel of the final image contains spectral information. **e.** Phasor plot of the spectral emission of ACDAN in solutions containing glycinin. The data for different protein concentrations (0, 0.1, 0.5, 1, 2, 5, 10 and 20 mg/mL) are superimposed. Increasing the protein-water ratio results in a blue shift of the emission, i.e. a decrease in water dipolar relaxation. The inset shows the full spectral phasor plot and the dashed line delineates the fragment which is magnified in the graph. The colors of the pixel clouds indicate the pixel density, increasing from blue to red. Note that ideally the phasor should be a point, but instead a distribution around a central point is obtained. **f.** Dipolar relaxation fraction histogram from two-cursor analysis for the data shown in **e**. Data are

represented as the mean (dots and lines) \pm SD (shadowed contour), $n=5$ per condition. The inset shows the trajectory displayed by the pixel clouds taken from the phasor plot, from which the histograms were calculated. **g.** The center of mass of the histograms for the dipolar relaxation fraction shown in **f** is represented as mean \pm SD (see eq. 5).

At low salt concentrations (< 43 mM), glycinin solutions are homogeneous (region R1 in Fig. 2a), but undergo liquid-liquid phase separation at higher salinity (from 43 to 230 mM, region R2), forming condensates of micrometric size (Fig. 2b), as previously reported^{35, 36}. Further increasing the salt concentration leads to the dissolution of the condensates and a reentrant homogeneous phase (R3 in Fig. 2a)^{35, 36}. We tested whether ACDAN hyperspectral imaging and phasor analysis can be used to probe the physicochemical interior of glycinin condensates and solutions at increasing salt concentration. Figure 2c shows the obtained spectral phasor plot, in which the combined data at different salinity fall mainly into two clouds. This binary behavior indicates two very different molecular environments for ACDAN when the protein is phase separated (region R2) or in a homogeneous phase (R1 and R3). It is important to remark that when phase separation takes place, ACDAN preferentially partitions in the condensates, giving almost no signal from the protein-poor phase. The histograms of the dipolar relaxation fraction and the corresponding center of mass are displayed in Figure 2d and e, respectively. The data for both of the homogeneous phase regions (R1 and R3) are located at high dipolar relaxation fractions (above 0.5), while the data from condensates (R2) are consistently low (below 0.5). As shown in Fig. 2d-e, there is a pronounced decrease of dipolar relaxation occurring with the onset of phase separation, reaching a minimum value at 75 mM NaCl and then reversing towards higher dipolar relaxation values. These results show not only that ACDAN senses increased crowding and constrained water relaxation in condensates (R2) compared to the homogeneous phases (R1 and R3), but it can also be sensitive to changes within the condensate phase at different conditions (see zoomed plots in Fig S1).

An additional feature of the phasor approach is the reciprocity principle^{37, 38}, by which a continuous color scheme (see color bar in Fig 2d) can be used to paint the images according to the phasors distribution (Fig. 2f), providing a qualitative visualization of the changes taking place. Here the same trend obtained with the quantification is observed: dipolar relaxation decreases with increasing salinity, reaching a maximum (more purple colored pixels) at 75mM NaCl and then reversing to a more polar environment (red colored pixels). Altogether, ACDAN dipolar relaxation quantification shows that this probe and the phasor approach are sensitive to liquid-liquid phase separation and report on different nano-environments within the different conditions, even for the homogeneous phases.

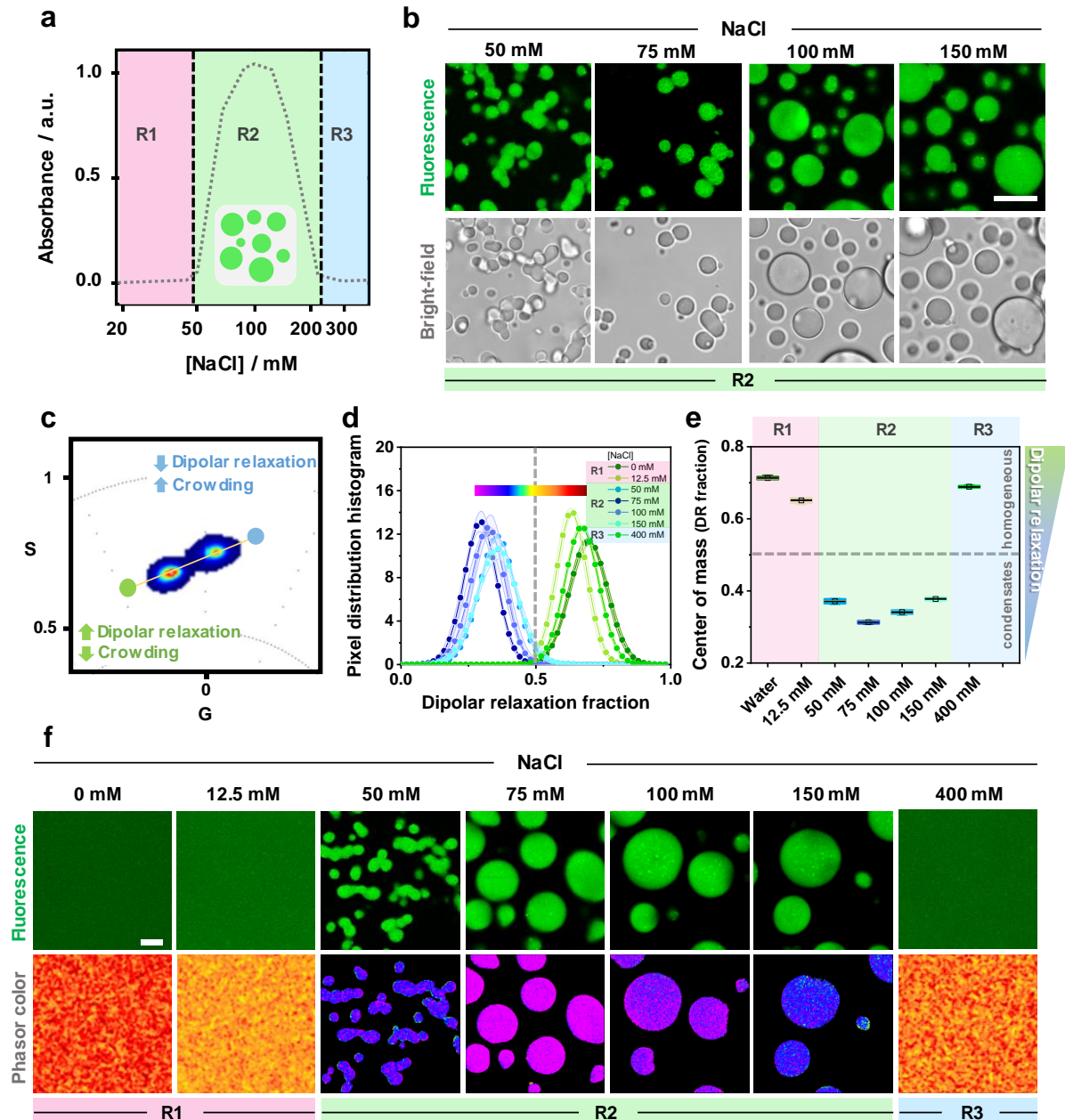


Figure 2. Characterization of glycinin condensates using ACDAN fluorescence spectral phasor approach.

a. Glycinin (10 mg/mL) exhibits phase separation at intermediate NaCl concentrations as shown from absorbance measurements. In regions R1 and R3 glycinin solutions are homogeneous, while in R2, phase separation occurs (data adapted from Chen et al. ³⁵). **b.** Confocal cross sections and brightfield images of glycinin condensates at different NaCl concentrations (within region R2 in a). Scale bar: 10 μ m. **c.** ACDAN spectral phasor plot for glycinin in water and in salt solutions at NaCl 12.5 mM, 50 mM, 75 mM, 100 mM, 150 mM and 400 mM. The data for the different conditions fall into two main pixel clouds. **d.** Histograms obtained from the two-cursor analysis showing the distribution of pixels along the line depicted in c. From the blue circular cursor to the green circular cursor crowding decreases and dipolar relaxation increases, and it is plotted as fraction. An arbitrary line was placed at $x=0.5$ to separate the two groups of data corresponding to homogeneous (R1, R3) and condensate (R2) regions in the phase diagram. Each histogram is shown as mean \pm SD, $n=5$ per condition. The continuous color bar used to paint images in (f) is shown on top of the histograms. **e.** Center of mass of the distributions shown in e for glycinin in water and at the indicated NaCl concentrations. When the system is homogeneous, data falls above $x=0.5$ (horizontal dashed line), indicating stronger dipolar relaxation. When the system is phase separated, the data points to weaker dipolar relaxation (crowded environment). Zoomed plots of d and e can be found in Fig. S1, showing that ACDAN emission changes at the different conditions, suggesting that the protein organization or structure in both, the condensates and the homogeneous phase is changing at the different NaCl concentrations. **f.** Examples of

ACDAN fluorescence intensity images (upper panel) and the same images colored using the continuous coloring scheme shown in d. Scale bar: 5 μ m.

Protein secondary structure rearrangements modify the water dynamics in condensates

Glycinin is a hexamer with two symmetric trimers stacked together with a total molecular weight of 360 kDa³⁹. Each monomer has an acidic and a basic polypeptide linked by a single disulfide bridge³⁹. The mechanism of glycinin phase separation implies molecular rearrangements between the basic and acidic residues³⁵. However, this mechanism is very general, and detailed structural changes in the protein between and within the different regions shown in Fig. 2a have not been explored. In order to understand how the changes sensed by ACDAN are related to protein structural rearrangements, we used label-free spectroscopic techniques, namely FTIR-ATR and Raman microscopy. These tools provide information on the protein secondary structure and the environment within the condensates. Figure 3a shows examples of the protein Amide I band obtained by FTIR-ATR for the different regions (R1, R2 and R3, see Fig. 2). When glycinin phase separates (R2), the band shifts towards higher wavenumbers (see inset in Fig. 3a), and subsequently shifts towards lower wavenumbers for the reentrant homogeneous phase (R3). These shifts imply structural changes in the protein at the different conditions. Such changes become more evident when taking the second derivative of the spectra (see Fig. S3a). Figure 3b summarizes the secondary structure percentage content of glycinin at the different NaCl concentrations (see methods and Fig. S2 and S3 for details). The changes occurring at the different conditions can be more clearly appreciated by plotting the percentage of secondary structure content of glycinin in each condition relative to the one of glycinin in the absence of NaCl, as showed in Fig. 3c. Upon phase separation, the percentage of random coil motifs increases, the alpha-helix content decreases, while the beta-sheet content changes are less pronounced and do not show a clear trend (Fig. S3b). The increase in random coils with the onset of phase separation is expected since this process is usually driven by the interaction of intrinsically disordered regions within proteins^{40, 41, 42}. After reaching a maximum, the secondary structure motifs of glycinin return to percentage values similar to the structure observed in the absence of NaCl. Notice that at high and low salinity, the secondary structure content of the protein is similar but different from the structure in water. This result supports the ACDAN data, which showed different spectral behavior at different salt concentrations even within the homogeneous regions (R1, R3).

Considering that ACDAN is sensitive to water dipolar relaxation and that the protein secondary structure is changing at different salt concentrations, it is likely that the confined water inside the condensates also alters its properties in turn^{27, 28, 43}. In this sense, Raman spectroscopy

allows measuring changes in the collective structure of water by observing changes in the OH vibrations engaged in hydrogen-bonding^{43, 44}. While in FTIR the water band interferes with the protein signal, in Raman the signal for the water OH vibrations appears at higher wavenumbers, away from the protein fingerprint region. Furthermore, when combined with microscopy, Raman spectroscopy provides images in which each pixel contains spectral information. Once obtained, it is possible to color the image according to the intensity of a given spectral band. Figure 3d shows the Raman image of a condensate part and the continuous phase surrounding it colored according to the band intensities of Amide I (1600-1700 cm^{-1}) and water (3000-3700 cm^{-1}). The water band intensity decreases towards the interior of the condensate while the protein one increases in the same direction (see color bar and intensity profiles in Fig. 2d). This result is understandable as protein/water ratio is higher in the condensates compared to the continuous phase. However, when analyzing the spectra for the different conditions, we noticed that not only the intensity of the water band changed, but also the contribution of the bands corresponding to different hydrogen bonding states⁴⁴ (see Fig. S4c). The two main contributions in the water band correspond to tetra-coordinated and di-coordinated water molecules and are located at 3225 cm^{-1} and 3432 cm^{-1} , respectively⁴⁴. In liquid water, the 3432 cm^{-1} band is predominant, but e.g. when water freezes, the 3225 cm^{-1} becomes dominant, causing a spectral shift to lower wavenumbers due to the increased strength of the tetra-coordinated hydrogen bonding⁴⁵. The intensity changes together with the Raman spectral shift can be quantified by using the generalized polarization function (GP, see Methods), which provides information on the water collective behavior⁴³. Figure 3d shows that the GP for the Raman water band increases with salt concentration, presenting a maximum at 100 mM NaCl and decreasing at higher salinity. Altogether, these results indicate that the changes in the protein secondary structure modulate the degree of water hydrogen bonding, and that ACDAN is responsive to these nano-environmental changes occurring in its immediate surrounding (compare the trends in Figs. 2e and 3e), providing a fingerprint of the condensate state at different stages of the phase separation process.

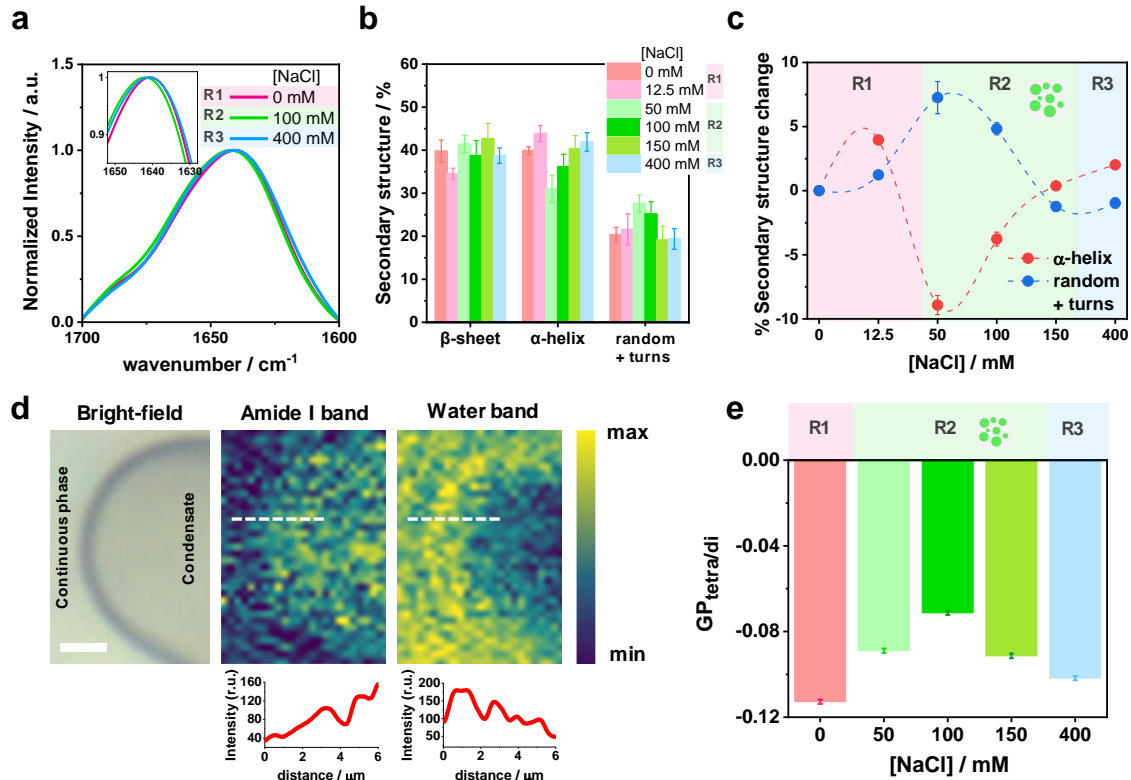


Figure 3. Glycinin secondary structure changes with salt concentration modifying the water environment inside condensates. **a.** Examples of FTIR-ATR spectra of the Amide I band of glycinin (10 mg/ml) at the different regions indicated in Fig. 2a, R1 (0 mM NaCl), R2 (100 mM NaCl), R3 (400 mM NaCl), see Fig. S2 and S3 for details. The inset shows a zoomed region highlighting the spectral shifts. **b.** Secondary structure content for glycinin at different conditions obtained by ATR-FTIR analysis. **c.** Percentage of secondary structure motifs for the different salinity conditions relative to the structure of glycinin in water. Major secondary structure rearrangements of the protein while changing salinity are associated with the α -helix and random/turns content. The most pronounced changes occur when glycinin enters the phase transition region (R2) showing an increase in random coils and a decrease in α -helical structures. Data showed as mean \pm SD, n=3. **d.** Raman microscopy image of a section of a single condensate at 100 mM NaCl. Pixels are colored according to the intensity of the Amide I band (middle image) or water band (right) as indicated by the color bar. The Amide I band increases and the water intensity decreases when approaching the interior of the condensate. Intensity profiles shown below the images were acquired along the white dashed lines in the images. Note that the lack of step-wise trend due to out-of-focus signal. Scale bar is 3 μ m. **e.** Spectral changes in the Raman water band quantified with the GP function calculated for the intensity contributions of the bands at 3225 and 3432 cm⁻¹ corresponding to tetra-coordinated and tri-coordinated water molecules (GP_{tetra/di}), see eq. 6. The observed changes indicate that the degree of hydrogen bonding of water is modified by the structural rearrangements of the protein at the different NaCl concentrations (see Fig. S4 for further details). Data showed as mean \pm SD, n=3.

Dehydration and lipid packing increase upon membrane wetting by biomolecular condensates

Protein condensates can wet membranes, promoting their remodeling²⁶. However, a molecular view of this interaction is still missing. We have previously shown that glycinin wetting affinity to membranes is enhanced at higher NaCl concentration²⁶. Here we use LAURDAN, the DAN probe including a lipid (lauroyl) chain (see Fig. 1a), to investigate the effect of wetting on molecular rearrangements in the membrane. Like ACDAN, the LAURDAN fluorescence spectrum is sensitive to the extent of the water dipolar relaxation process around

the probe moiety³⁴. The mechanism of LAURDAN fluorescence in lipid membranes has been extensively discussed and reviewed for more than 30 years^{31, 34, 46, 47}. LAURDAN fluorescence is responsive to the dynamics of a few water molecules within the region where it is located in the bilayer (nearby the glycerol backbone of the glycerophospholipids)³⁴. For this reason, LAURDAN has been widely used to assess the membrane phase state and hydration level^{31, 34, 43, 48, 49}. Thus, we exploited LAURDAN sensitivity to address the effect of condensate wetting on membrane packing and hydration. Figure 4a shows a scheme of the different partial wetting morphologies that can be obtained when condensates interact with GUVs²⁶. The wetting is characterized by the change in the contact angles^{21, 26} (Fig. 4a). The bottom panel in Fig. 4a shows examples of DOPC GUVs in contact with condensates at different NaCl concentrations. It can be seen that when increasing the salt concentration the condensates spread more on the vesicles, meaning that the wetting is stronger²⁶. We labeled the membranes with LAURDAN and applied the spectral phasor analysis to these membrane-condensate systems. Using the two-cursor analysis, we could separate the contributions of the membrane in contact with the condensate from the condensate-free (bare) membrane at a single vesicle level, as shown in Fig. 4b. Remarkably, the membrane in contact with the condensate displays an increased lipid packing (indicated as lower fluidity fraction in Fig 4b) the rest of the membrane compared to the bare membrane. Next, we evaluated how this effect changes when the interaction between the membrane and the condensate is stronger, i.e. when the membrane wetting increased. Figure 4c shows the fluidity fraction histograms and the corresponding center of mass for the membrane segments in contact with condensates with increasing salt concentration/increasing wetting. The analysis shows that increasing the wetting strength results in higher lipid packing and membrane dehydration. In contrast, the effect on the condensate-free membrane segment is negligible (Fig. 4d).

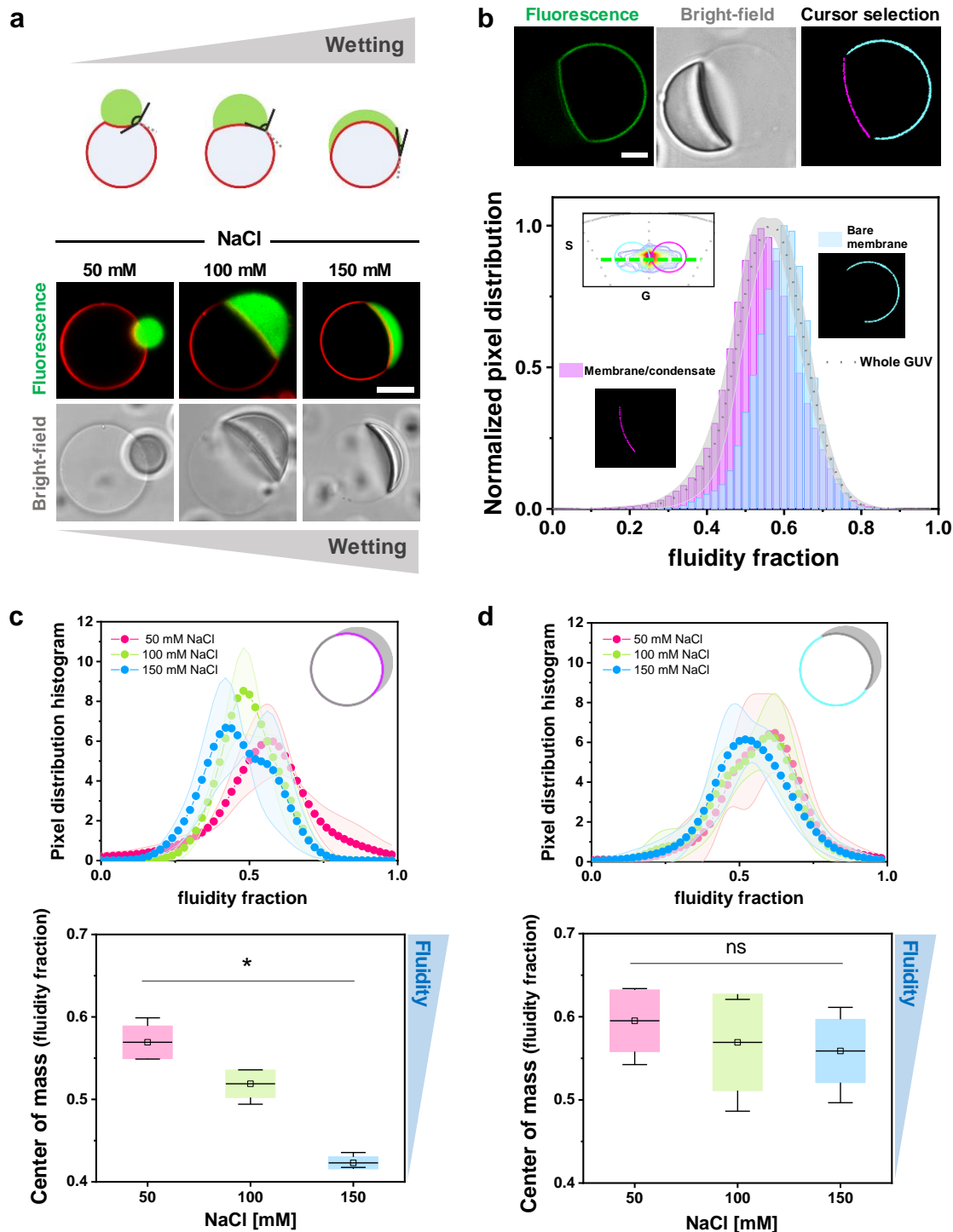


Figure 4. Membrane wetting by condensates correlates with an increase in lipid packing and membrane dehydration. **a.** Biomolecular condensates can wet membranes^{21, 26}, and the increase in wetting can be observed as an increase in the spreading of the droplet over the membrane, and a decrease in the contact angle as exemplified in the sketch (upper panel). Examples of membrane wetting (DOPC GUVs labeled with 0.1 mol% Atto 647N-DOPE) by glycinin condensates (FITC labelled) at the indicated NaCl concentrations (bottom panel). Scale bar: 10 μ m. **b.** Using LAURDAN fluorescence spectral phasor analysis, we can segment the vesicle and separate the contributions of the membrane in contact with the condensate and the bare membrane on the same GUV. Example of a single vesicle analysis for a DOPC GUV labelled with 0.5% LAURDAN in contact with an unlabeled condensate (at 100 mM NaCl). The cursor-colored segments and the corresponding histograms are shown in the bottom panel. Here it is shown that the part of the membrane in contact with the condensate is more packed (with lower fluidity fraction) than the bare membrane. Here distributions were normalized for clarity. Scale bar: 10 μ m. **c-d.** Histograms of the pixel distribution (top panel), and center of mass of the distributions (bottom panel) for the

membrane segment in contact with the condensate (c) and for the bare membrane segment (d), at the indicated NaCl concentrations. The sketches indicate the part of the membrane being analyzed. Data is shown as mean \pm SD (n=5 GUVs per condition). Differences are significant p<0.05, ANOVA and Tukey post-test analysis.

Hydration and packing changes are a common feature of membrane-condensate interactions

To test whether the performance of LAURDAN as a fluidity sensor in wetted membranes is universal and whether the observed changes are independent of the condensate system, we evaluated the effect of wetting on membrane packing in the well-studied aqueous two-phase system (ATPS) consisting of a mixture of PEG and Dextran^{21, 23}. Membranes encapsulating ATPS can undergo liquid-liquid phase separation upon deflation of the vesicles. This is achieved by increasing the osmolarity of the external milieu: water is expelled out to the vesicle due to the osmotic gradient, and in consequence, the polymers become concentrated on the inside, driving the phase separation^{50, 51}. We used a microfluidic setup⁵¹ that allows us to work at single-vesicle level and exchange the buffer conditions in a stepwise and controlled manner. In Fig. 5a, the degree of deflation r indicates the ratio between the osmolarity outside and inside the vesicles. Initial deflation produces the formation of membrane tubes toward the inside of the vesicle (the tubes are stabilized by spontaneous curvature generation from asymmetric PEG adsorption⁵²). However, after phase separation occurs ($r \geq 1.3$), a further deflation produces bud formation and nanotubes accumulation on the interface between the phase-separated polymers^{50, 51}. These morphological changes are the product of the wetting transition of the polymers-rich phase within the membrane^{21, 53}, with wetting increasing as the deflation ratio r increases (Fig. 5a).

Here, we used LAURDAN fluorescence with FLIM and the phasor analysis to unravel the changes in lipid packing and hydration. This methodology presents an advantage over the spectral phasor approach since, given the photophysics of LAURDAN, we can independently study the polarity and the water dipolar relaxation changes by using two channels for collecting the emission signal (see Methods)^{31, 43, 54, 55, 56}. In addition, the acquisition mode of FLIM allows the accumulation of several frames, providing a reasonable resolution that was crucial for the case of ATPS systems since they presented a low signal-to-noise ratio. . The measurements in the blue channel (see Methods) provide information on the polarity changes related to the increase in membrane packing/fluidity, while the green channel gives information regarding the dipolar relaxation. Figure 5b shows the changes in the fluidity fraction for the ATPS vesicle systems. For this system, the analysis was performed taking into account the whole membrane, since we did not find significant differences for different membrane segments (data not shown). A correlation between the increase in wetting and the decrease in the fluidity fraction is observed. Note that for the first deflation step ($r=1.1$) there are not significant

differences compared to the initial state, but the effect is pronounced when phase separation occurs ($r \geq 1.3$). For comparison, Fig. 5c shows the results obtained for the glycinin condensates in contact with membranes obtained with FLIM (corresponding to the wetted membrane segment). These results corroborate the data obtained with spectral phasor analysis (Fig. 4) demonstrating the robustness of the method. Regarding the dipolar relaxation analysis (as obtained from the green channel), Figs. 5d and 5e show the results for the ATPS and the glycinin condensates in contact with GUVs, respectively. For both systems, the water dipolar relaxations were reduced at increased wetting. These results indicate that water dynamics around LAURDAN are reduced for both analyzed systems when membrane wetting increases.

By using two very different systems displaying changes in membrane wetting, and different spectroscopic methods, namely hyperspectral imaging and FLIM, we observed a similar phenomenon regarding lipid packing and membrane hydration, strongly suggesting that this could be a general phenomenon of membrane wetting by biomolecular condensates.

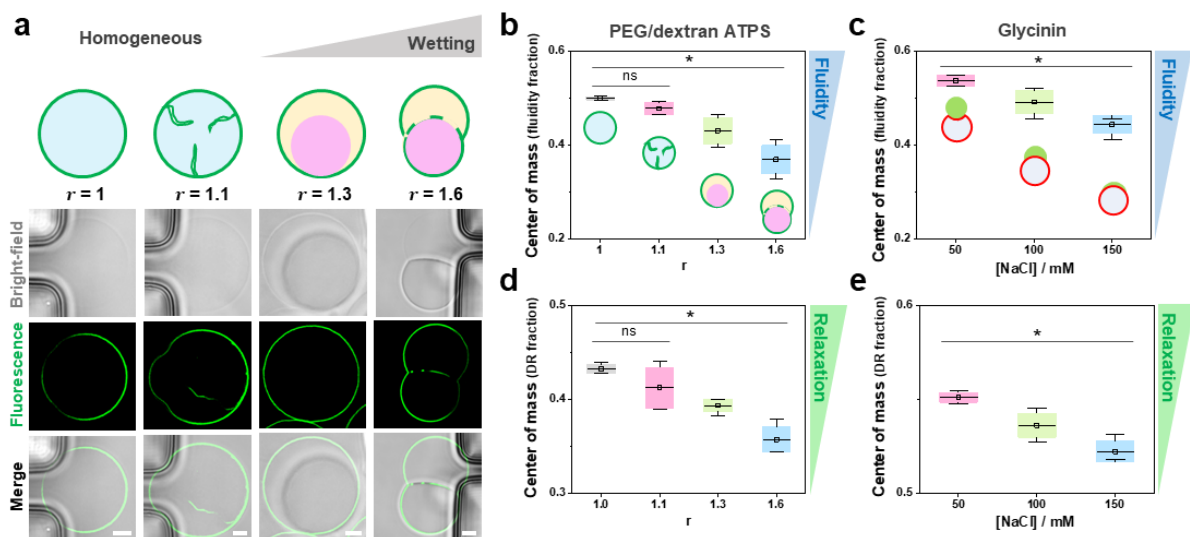


Figure 5. Membrane dehydration and increased packing are general features of wetting by phase-separated droplets. **a.** DOPC vesicles filled with a PEG/Dextran solution (ATPS) undergo morphological transformations due to the increase in membrane wetting affinity by the polymer-rich phases. Phase separation inside the GUV is achieved by increasing the external osmolarity and consequently raising the polymer concentration inside the vesicle, which leads to liquid-liquid phase separation (see methods for further details). The dextran-rich phase (pink color in the sketch) is denser and has a higher refractive index⁵⁷ than the PEG-rich phase (yellow), as can be observed in the bright-field images. The degree of vesicle osmotic deflation is given by the ratio of the external to initial internal osmolarity, r . Scale bars: 5 μm . **b-e.** FLIM phasor fluidity and dipolar relaxation analysis for DOPC GUVs labelled with 0.5% LAURDAN in contact with the ATPS (**b, d**) and the glycinin condensates (**c, e**), respectively. The center of mass for fluidity changes (top panel) and dipolar relaxation changes (bottom panels) are shown. Histograms can be found in Fig. S5. In both condensate systems, an increase in membrane wetting leads to a decrease in fluidity. Differences are significant $p < 0.05$, ANOVA and Tukey post-test analysis. For no significant differences, “ns” is indicated.

Discussion

Membrane wetting by biomolecular condensates has lately emerged as an exciting field as it is involved in very different processes occurring in cell organization, development, and degradation⁷. Although membrane morphological transformations by condensate wetting transitions were first described many years ago²¹, it was very recently that the biological relevance of membrane-condensate interactions came to the spotlight^{7, 8, 58, 59}. This quest highlights the use of *in-vitro* models for the careful control, monitoring and tuning of the physicochemical properties to understand membrane condensate interactions fully. In this direction, we have recently performed a systematic study of membrane wetting by biomolecular condensates by using glycinin condensates in contact with GUVs²⁶. However, membrane condensate interactions are complex, and the molecular mechanism behind these interactions remains poorly investigated. Here, we resolve the mechanism at a molecular scale by using state-of-the-art fluorescent approaches to exploit the properties of two powerful nano-environmental sensors. First, we demonstrated that the spectral phasor analysis of ACDAN fluorescence within the condensates can provide key information on the phase separation process. The results revealed that ACDAN response is very sensitive to protein structural rearrangements, since they modify the water environment surrounding the probe moiety. The approaches we introduce present a powerful tool for investigating condensate structural properties. On the one hand, we have demonstrated that there are secondary structure rearrangements in the different stages of salt-driven phase separation (Fig. 3 a, b), revealing the high responsiveness of these structures to slight changes in conditions such as salinity, pH, or temperature. On the other hand, Raman experiments show that the collective structure of water is being modified in the condensates environment. Raman spectroscopy has already been used to determine protein concentration and measuring structural heterogeneity in single droplets^{60, 61}. Additionally, our results indicate that Raman microscopy can be a powerful tool for getting insight into the phase separation process, and to monitor changes occurring at different stages.

It is essential to highlight that ACDAN spectroscopic properties can supplement the current set of techniques^{20, 62} for measuring condensates properties. This is particularly relevant considering that most of the commercial confocal microscopes nowadays are capable of performing hyperspectral imaging⁶³.

In general, protein intrinsic fluorescence, normally governed by the fluorescence of tryptophan residues, could report on structural changes taking place at different conditions^{64, 65}. However, given the complexity of biomolecular condensates, intrinsic fluorescence is in general not suitable to evaluate changes occurring during phase separation, and extrinsic probes must be used for spectroscopic studies^{65, 66, 67}. In particular, glycinin has 24 tryptophan residues, most of them hidden within the hydrophobic core, making autofluorescence unsuitable for

evaluating the changes explored in this work (see Fig. S6). In this manner, ACDAN has proven to be an excellent extrinsic reporter for the study of condensates, since the measurement of water dipolar relaxation, provides a fingerprint of a given state of the condensates. In this sense, it has been recently reported that ACDAN can distinguish between condensates formed by Dengue and Zika virus capsid proteins and RNA¹². The combination of ACDAN fluorescence with the phasor approach could also constitute a quick and sensitive method for evaluating chemical changes within the condensates upon the addition of different components, like drugs⁶⁸ to modulate the phase separation process. Additionally, it could be applied for the prediction and the evaluation of biomolecules partition⁶⁹.

Previously, we have demonstrated that the membrane wetting by condensates can be regulated by tuning simple parameters like the salinity of the medium or the membrane composition.²⁶ Additionally, it has been reported that membranes can regulate the assembly and nucleation of condensates^{14, 15}. However, to the best of our knowledge, there are no studies aiming to elucidate the mechanism behind the membrane-condensate interaction. Here, by using LAURDAN hyperspectral imaging and FLIM together with the phasor analysis, we explored the membrane molecular changes determined by the wetting with biomolecular condensates. We proved that the membrane in contact with the condensate exhibits increased lipid packing, and is more dehydrated than the bare condensate-free membrane (Fig. 4b). In this sense, it has been shown that in presence of macromolecular crowding, the interface of membranes becomes dehydrated as a result of the reduced activity of water, making even possible the transition between different lyotropic phases⁴³. This further corroborates our finding that the membrane in contact with the condensate, that provides a highly crowded interface, shows a more packed and dehydrated state. In the same direction, the hydration state of lipids has been recently shown to have a direct impact on membrane fluidity⁷⁰, and the diffusion coefficient of the membrane in contact with condensates has proven to be slower than for the bare membrane^{26, 71}.

Remarkably, when increasing the interaction between the membrane and the condensate (i.e. by increasing wetting), the membrane becomes less fluid and more dehydrated in consequence (Fig. 4c). By exploiting FLIM capabilities of distinguishing between the polarity/fluidity changes and the water dipolar relaxation effect, we tested a well-known polymer system that undergoes liquid-liquid phase separation inside vesicles upon deflation (Fig. 5a). In this system of vesicles encapsulating ATPS, wetting between the polymers and the membrane is increased by sequential deflation steps. Again, we saw that increasing wetting correlates with an increase in membrane lipid packing and dehydration (Fig. 5b), and that water dynamics is also decreasing (Fig. 5d). These results present the same trend as the one obtained for the protein condensates (Fig. 5c,e). Altogether, our results suggest that membrane dehydration and increased packing is a general mechanism characterizing

membrane wetting by biomolecular condensates. This constitutes a convenient way in which cells could tune membrane packing by changing the wetting affinity of the condensates. It would be interesting to explore in future studies the effect of wetting in complex lipid mixtures containing cholesterol, to assess the influence of the membrane phase state on wetting and the possible sorting of lipids in the region of interaction.

In this work, we provided new information on the molecular scale for the wetting of membranes by biomolecular condensates. Surely, understanding why the interaction with the condensates is different in each condition is far more complex. We showed that the protein secondary structure changes between the different conditions, leading to different specific interactions with the membrane. Future studies should further focus on this direction to completely understand the crosstalk between the membrane and biomolecular condensates.

Methods

Materials. 1,2-dioleoyl-sn-glycero-3-phosphocholine (DOPC) was purchased from Avanti Polar Lipids (IL, USA). 6-acetyl-2-dimethylaminonaphthalene (ACDAN) was purchased from Santa Cruz Biotechnology (USA), and 6-dodecanoyl-2-dimethylaminonaphthalene (LAURDAN) from Thermofisher Scientific (USA). ATTO 647N-DOPE was obtained from ATTO-TEC GmbH (Siegen, Germany). Polydimethylsiloxane (PDMS) and the curing agent were obtained as SYLGARD® 184 silicone elastomer kit from Dow Corning (Michigan, USA). Dextran from *Leuconostoc* spp (Mw 450-650 kg/mol), and poly(ethylene glycol) (PEG 8000, Mw 8 kg/mol) were purchased from Sigma-Aldrich. Chloroform obtained from Merck (Darmstadt, Germany) was of HPLC grade (99.8 %). The lipid stocks were mixed as chloroform solutions at 4 mM, contained 0.1 mol% ATTO 647N-DOPE or 0.5 mol% LAURDAN, and were stored until use at -20°C. Fluorescein isothiocyanate isomer (FITC), sucrose, glucose, dimethyl sulfoxide (DMSO), sodium hydroxide (NaOH) and sodium chloride (NaCl) were obtained from Sigma-Aldrich (Missouri, USA). All solutions were prepared using ultrapure water from SG water purification system (Ultrapure Integra UV plus, SG Wasseraufbereitung) with a resistivity of 18.2 MΩ cm.

Vesicle preparation and deflation. DOPC giant unilamellar vesicles containing 0.5 mol % LAURDAN were prepared by electroformation as described elsewhere⁷². Briefly, 2-4 μL lipid solution were spread onto indium tin oxide (ITO)-coated glasses and dried under vacuum for 1 h. The plates were assembled into a chamber with a Teflon spacer and the swelling solution (1.9 mL) was introduced. For electroformation, a sinusoidal electric field of 1.0 Vpp and 10 Hz was applied using a function generator for 1.5 h. For the studies with glycinin condensates, a sucrose solution was used for swelling, and once formed, the vesicles were diluted 1:1 in a glucose solution of the same osmolarity before use. In all cases, osmolarities of sucrose/glucose solutions matched the osmolarities of the condensate NaCl solutions (100-300 mOsm). The solution osmolarities were carefully adjusted using a freezing-point osmometer (Osmomat 3000, Gonotec, Germany)

The procedure for ATPS preparation and vesicle deflation together with the PEG/dextran phase diagram are described in detail in Zhao et al.⁵¹. Briefly, the swelling solution consisted of a mixture of dextran and PEG with initial weight ratio dextran:PEG = 1.57:1 (4.76% and 3.03% weight fractions, respectively). Afterward, the GUVs containing ATPS were dispersed into an isotonic polymer solution with lower density (dextran:PEG 1:1, 3.54%, 3.54% weight fractions) to facilitate their sedimentation. Vesicle deflation was controlled via a NeMESYS high-precision syringe pump (CETONI GmbH) by exchanging the external medium with a

series of different hypertonic solutions containing constant polymer weight fractions and an increased weight fraction of sucrose.

Microfluidics. The microfluidic device consists of a cascade GUV trapping system, which is described in detail elsewhere⁵¹. It was produced using PDMS pre-cursor and curing agent (Sylgard 184, Dow Corning GmbH), at a mass ratio of 10:1. After polymerization at 80 °C for 2 hours, inlet and outlet holes were punched with a biopsy punch with a plunger system (Kai Medical). Then the PDMS chips and glass coverslips were treated with plasma for 1 min using high-power expanded plasma cleaner (Harrick Plasma), and bonded together afterward. Before the experiments, the desired amount of solution was filled into the microfluidic device by centrifugation at 900 relative centrifugal force (Rotina 420R, Hettich). Solution exchange was performed with a NeMESYS high-precision syringe pump, at a flow speed of 1 $\mu\text{L}/\text{min}$ for 40 minutes to ensure at least 10 times exchange of the internal volume of the microfluidic device ($\sim 4 \mu\text{L}$). For imaging, the flow speed was 0.035 $\mu\text{L}/\text{min}$ to prevent vesicle movement.

Protein extraction, purification, and labeling. Glycinin was purified as described in Chen et al.³⁵. Briefly, defatted soy flour was dispersed in 15-fold water in weight and adjusted to pH 7.5 with 2 M NaOH. After centrifugation (9000 $\times g$, 30 min) at 4°C, dry sodium bisulfite (SBS) was added to the supernatant (0.98 g SBS/L). The pH of the solution was adjusted to 6.4 with 2 M HCl, and the obtained turbid dispersion was kept at 4 °C overnight. Next, the dispersion was centrifuged (6500 $\times g$, 30 min) at 4 °C. The glycinin-rich precipitate was dispersed in 5-fold water, and the pH was adjusted to 7. The glycinin solution was then dialyzed against Millipore water for two days at 4 °C and then freeze-dried to acquire the final product with a purity of 97.5%³⁵.

To label the protein, 20 mg/mL soy glycinin solution was prepared in 0.1 M carbonate buffer (pH 9). A 4 mg/mL solution of FITC dissolved in DMSO was slowly added to the protein solution with gentle stirring to a final concentration of 0.2 mg/mL. The sample was incubated in the dark while stirring at 23 °C for 3 h. The excess dye was removed using a PD-10 Sephadex G-25 desalting column (GE Healthcare, IL, USA), and the buffer was exchanged for ultrapure water. The pH of the labeled protein solution was adjusted to 7.4 by adding 0.1 M NaOH. For fluorescence microscopy experiments, an aliquot of this solution was added to the working glycinin solution to a final concentration of 4%v/v.

For ACDAN hyperspectral imaging, the dye was directly added to the protein solution (unlabeled) before the experiment to a final concentration of 5 μM .

Condensates formation. A glycinin solution at 20 mg/mL pH=7 was freshly prepared in ultrapure water and filtered with 0.45 μm filters to remove any insoluble materials. To form the

condensates, the desired volume of the glycinin solution were mixed with the same volume of a NaCl solution of twice the desired final concentration. In this manner, the final concentration was 10 mg/mL; this is the optimized concentration for obtaining micrometric size condensates^{26, 35}.

Glycinin condensates in contact with membranes. The vesicle suspension was diluted 1:10 in a NaCl solution with the final NaCl concentration matching the one of the condensates. The condensate suspension was diluted 1:4 and added to the vesicle suspension at a 15% v/v (condensate / GUV suspension). After gently mixing the vesicle-condensate suspension, an aliquot of 100 μ L was placed on a coverslip (26 \times 56 mm, Waldemar Knittel Glasbearbeitungs GmbH, Germany) for confocal microscopy and a chamber was formed using a round spacer and closing coverslip. The coverslips were previously washed with ethanol and water and passivated with a 10 mg/mL BSA solution.

Hyperspectral imaging and fluorescence lifetime imaging microscopy (FLIM). Hyperspectral and FLIM images were acquired using a confocal Leica SP8 FALCON microscope equipped with a 63x, 1.2 NA water immersion objective (Leica, Mannheim, Germany). The microscope was coupled to a pulsed Ti:Sapphire laser MaiTai (SpectraPhysics, USA), with a repetition rate of 80 MHz. A two-photon wavelength of 780 nm was used for ACDAN and LAURDAN excitation. Image acquisition was performed with a frame size of 512 \times 512 pixels² and a pixel size of 72 nm. For hyperspectral imaging the xy λ configuration of the Leica SP8 was used, sequentially measuring in 32 channels with a bandwidth of 9.75 nm in the range from 416 to 728 nm. The FLIM data acquisition was performed by high-precision single-molecule detection hybrid detectors (HyD SMD, Leica) with GaAsP photocathodes. For the blue channel, the detection was set in the range of 416-470 nm, and for the green channel, 500-600 nm (see Fig. S5). In all cases, 10-20 frames were accumulated. FLIM calibration of the system was performed by measuring the known lifetime of the fluorophore Coumarin 6 (100nM) in ethanol (2.5 ns⁷³). Hyperspectral and FLIM images were processed by the SimFCS software developed at the Laboratory of Fluorescence Dynamics, available on the webpage (<https://www.lfd.uci.edu/globals/>).

Spectral phasor plot. The fluorescence spectra at each pixel were transformed to polar coordinates and plotted in Cartesian space according to:

$$G(\lambda) = \frac{\int_{\lambda_{min}}^{\lambda_{max}} I(\lambda) \cos\left(\frac{2\pi n(\lambda - \lambda_i)}{\lambda_{max} - \lambda_{min}}\right) d\lambda}{\int_{\lambda_{min}}^{\lambda_{max}} I(\lambda) d\lambda} \quad (1)$$

$$S(\lambda) = \frac{\int_{\lambda_{min}}^{\lambda_{max}} I(\lambda) \sin\left(\frac{2\pi n(\lambda - \lambda_i)}{\lambda_{max} - \lambda_{min}}\right) d\lambda}{\int_{\lambda_{min}}^{\lambda_{max}} I(\lambda) d\lambda} \quad (2)$$

where $I(\lambda)$ represent the intensity at every wavelength (channel), n is the number of the harmonic ($n=1$ for the data showed here) and λ_i the initial wavelength. The angular position in the spectral phasor plot relates to the center of mass of the emission spectrum and the modulus depends on the spectrum's full width at the half maximum (FWHM). A detailed description of spectral phasor plot properties can be found in Malacrida et al⁷⁴.

Lifetime phasor plot. For the lifetime phasor plot, the fluorescence decay $I(\tau)$ was acquired at each pixel of an image and the coordinates were calculated and plotted according to:

$$G(\tau) = \frac{\int_0^T I(\tau) \cos(\omega\tau) d\tau}{\int_0^T I(\tau) d\tau} \quad (3)$$

$$S(\tau) = \frac{\int_0^T I(\tau) \sin(\omega\tau) d\tau}{\int_0^T I(\tau) d\tau} \quad (4)$$

where ω is the angular modulation frequency, and $\omega = 2\pi f$, where f is the laser repetition frequency and T is the period of the laser frequency.

Two-cursor analysis. Exploiting the linear combination properties of the phasor plot³⁸, the two-cursor analysis was used in all cases to calculate the histogram for the pixel distribution along the line (as exemplified in Fig. 1f) for dipolar relaxation changes of ACDAN and LAURDAN. When using the term fluidity obtained from LAURDAN fluorescence, we are referring to the changes in the lipids order parameters⁴⁹, considering any process that can change the lipid rotational or translational rates. The histograms are presented as the number of pixels at each step along the line between the two cursors, normalized by the total number of pixels. We plotted the average value for each histogram \pm standard deviation, as well the center of mass of the histogram for quantitative analysis with descriptive statistics. The center of mass was calculated following:

$$CM = \frac{\sum_{i=0}^{i=1} F_i i}{\sum_{i=0}^{i=1} F_i} \quad (5)$$

where F_i is the fraction for fluidity or dipolar relaxation.

Attenuated total reflectance-Fourier transform infrared spectroscopy (ATR-FTIR). The spectra were acquired on a Vertex 70v spectrophotometer (Bruker Optik GmbH, Germany) equipped with a single reflection diamond reflectance accessory continuously purged with dried air to reduce water vapor distortions in the spectra. Samples (~3 μ L) were spread on a diamond crystal surface, and dried under nitrogen flow to obtain the protein spectra. Sixty four accumulations were recorded at 25°C using a nominal resolution of 4 cm^{-1} . Spectra were processed using Kinetic software developed by Dr. Erik Goormaghtigh at the Structure and Function of Membrane Biology Laboratory (Université Libre de Bruxelles, Belgium). After subtraction of water vapor and side chain contributions, the spectra were baseline corrected and the area normalized between 1700 and 1600 cm^{-1} . For a better visualization of the overlapping components arising from the distinct structural elements, the spectra were deconvoluted using Lorentzian deconvolution factor with a full width at the half maximum (FWHM) of 30 cm^{-1} and a Gaussian apodization factor with a FWHM of 16.66 cm^{-1} to achieve a line narrowing factor $K = 1.8^{75}$. In order to assign a determined band to the peaks in the spectra, a second derivative was performed on the Fourier self-deconvoluted spectra. The bands identified by both procedures were used as initial parameters for a least square iterative curve fitting of the original IR band ($K = 1$) in the amide I region, using mixed Gaussian/Lorentzian bands. Peak positions of each identified individual component were constrained within $\pm 2 \text{ cm}^{-1}$ of the initial value. Details on the band assignment and the fitting can be found in Table S1 and Figs. S2 and S3.

Raman Microscopy. Raman images and spectra were acquired with a Raman confocal microscope Alpha300 R (WITec GmbH, Germany). The objective was a Zeiss EC Epiplan 50x/0.75, The excitation wavelength 532 nm and the laser power 30 mW. Image size was 15x15 μm^2 with 35 points per line and 35 lines per image. Spectra were taken in the range 400-4100 cm^{-1} . The Raman band of the silicon wafer was used to calibrate the spectrometer. Data was analyzed with the Project FIVE data evaluation software from WITec. Spectral changes in the water band were quantified with the generalized polarization function $GP_{tetra/di}$ calculated from the intensity contributions of the bands at 3225 and 3432 cm^{-1} , corresponding respectively to tetra-coordinated and di-coordinated water molecules engaged in hydrogen bonds as previously reported⁴³:

$$GP_{tetra/di} = \frac{I_{3225} - I_{3432}}{I_{3225} + I_{3432}} \quad (6)$$

Here I_{3225} and I_{3432} represent the Raman intensities at the respective wavenumbers.

Data reproducibility and statistics. At least five independent replicates were used to perform the statistical analysis. Histograms are shown as means \pm standard deviation (SD). The center of mass are shown as box charts where the horizontal lines indicate the mean value, the box width indicates the SD and the whiskers the maximum and minimum values. Results were analyzed using ANOVA with Tukey post-test, where a $p < 0.05$ was considered statistically significant. Statistical analysis and data processing were performed with the software Origin Pro (Originlab corporation).

Author contributions

A.M., L.M. and R.D. conceived the experiments and designed the project. A.M. and M.S. performed the experiments. Z.Z. aided with the ATPS systems and microfluidic setup. A.M., M.S., and L.M. analyzed the data. A.M., L.M., and R.D. wrote the paper, with input from the rest of the authors.

Aknowledgements

A.M. acknowledges support from Alexander von Humboldt Foundation. Z.Z. acknowledges support from Free State of Thuringia (TAB; SARSRapid 2020-FGR-0051), and Deutsche Forschungsgemeinschaft (DFG, German Research Foundation) - project number 316213987 - SFB 1278 (project D01). L.M. was supported in part by PEDECIBA, FOCEM - Fondo para la Convergencia Estructural del Mercosur (COF 03/11) and as Imaging Scientist by grant number 2020-225439 from the Chan Zuckerberg Initiative DAF, an advised fund of Silicon Valley Community Foundation. The authors would like to thank Dr. Nannan Chen for providing the purified protein, and Dr. Clemens Schmitt for the aid with the Raman experiments. The authors would like to dedicate this work to the memory of Dr. Luis A. Bagatolli.

References

1. Banani SF, Lee HO, Hyman AA, Rosen MK. Biomolecular condensates: organizers of cellular biochemistry. *Nature Reviews Molecular Cell Biology* **18**, 285-298 (2017).

2. Ladouceur A-M, *et al.* Clusters of bacterial RNA polymerase are biomolecular condensates that assemble through liquid–liquid phase separation. *Proceedings of the National Academy of Sciences* **117**, 18540-18549 (2020).
3. Laflamme G, Mekhail K. Biomolecular condensates as arbiters of biochemical reactions inside the nucleus. *Communications Biology* **3**, 773 (2020).
4. Alberti S, Hyman AA. Biomolecular condensates at the nexus of cellular stress, protein aggregation disease and ageing. *Nature Reviews Molecular Cell Biology* **22**, 196-213 (2021).
5. Molliex A, *et al.* Phase Separation by Low Complexity Domains Promotes Stress Granule Assembly and Drives Pathological Fibrillization. *Cell* **163**, 123-133 (2015).
6. Iserman C, *et al.* Genomic RNA Elements Drive Phase Separation of the SARS-CoV-2 Nucleocapsid. *Molecular Cell* **80**, 1078-1091.e1076 (2020).
7. Kusumaatmaja H, May AI, Knorr RL. Intracellular wetting mediates contacts between liquid compartments and membrane-bound organelles. *Journal of Cell Biology* **220**, e202103175 (2021).
8. Snead WT, Gladfelter AS. The Control Centers of Biomolecular Phase Separation: How Membrane Surfaces, PTMs, and Active Processes Regulate Condensation. *Molecular Cell* **76**, 295-305 (2019).
9. Beutel O, Maraspini R, Pombo-García K, Martin-Lemaitre C, Honigsmann A. Phase Separation of Zonula Occludens Proteins Drives Formation of Tight Junctions. *Cell* **179**, 923-936.e911 (2019).
10. Agudo-Canalejo J, *et al.* Wetting regulates autophagy of phase-separated compartments and the cytosol. *Nature* **591**, 142-146 (2021).
11. Su X, *et al.* Phase separation of signaling molecules promotes T cell receptor signal transduction. *Science* **352**, 595-599 (2016).
12. Ambroggio EE, Costa Navarro GS, Pérez Socas LB, Bagatolli LA, Gamarnik AV. Dengue and Zika virus capsid proteins bind to membranes and self-assemble into liquid droplets with nucleic acids. *Journal of Biological Chemistry* **297**, 101059 (2021).
13. Lee JE, Cathey PI, Wu H, Parker R, Voeltz GK. Endoplasmic reticulum contact sites regulate the dynamics of membraneless organelles. *Science* **367**, eaay7108 (2020).
14. Snead WT, Jalihal AP, Gerbich TM, Seim I, Hu Z, Gladfelter AS. Membrane surfaces regulate assembly of ribonucleoprotein condensates. *Nature Cell Biology* **24**, 461-470 (2022).

15. Babl L, Merino-Salomón A, Kanwa N, Schwille P. Membrane mediated phase separation of the bacterial nucleoid occlusion protein Noc. *Scientific Reports* **12**, 17949 (2022).
16. Wan-Chih Su DG, Andrew Rowland, Christine Keating, Atul Parikh. Liquid-Liquid Phase Separation inside Giant Vesicles Drives Shape Deformations and Induces Lipid Membrane Phase Separation. *Research Square*, (2022).
17. Wang H-Y, *et al.* Coupling of protein condensates to ordered lipid domains determines functional membrane organization. *bioRxiv*, 2022.2008.2002.502487 (2022).
18. Cans AS, Andes-Koback M, Keating CD. Positioning lipid membrane domains in giant vesicles by micro-organization of aqueous cytoplasm mimic. *Journal of the American Chemical Society* **130**, 7400-7406 (2008).
19. Bergeron-Sandoval L-P, *et al.* Endocytic proteins with prion-like domains form viscoelastic condensates that enable membrane remodeling. *Proceedings of the National Academy of Sciences* **118**, e2113789118 (2021).
20. Wang Z, Lou J, Zhang H. Essence determines phenomenon: Assaying the material properties of biological condensates. *Journal of Biological Chemistry* **298**, 101782 (2022).
21. Li Y, Lipowsky R, Dimova R. Transition from complete to partial wetting within membrane compartments. *Journal of the American Chemical Society* **130**, 12252-12253 (2008).
22. Dimova R, Lipowsky R. Giant Vesicles Exposed to Aqueous Two-Phase Systems: Membrane Wetting, Budding Processes, and Spontaneous Tubulation. *Advanced Materials Interfaces* **4**, 1600451 (2017).
23. Dimova R, Lipowsky R. Lipid membranes in contact with aqueous phases of polymer solutions. *Soft Matter* **8**, 6409-6415 (2012).
24. Keating CD. Aqueous Phase Separation as a Possible Route to Compartmentalization of Biological Molecules. *Accounts of Chemical Research* **45**, 2114-2124 (2012).
25. Yuan F, *et al.* Membrane bending by protein phase separation. *Proceedings of the National Academy of Sciences* **118**, e2017435118 (2021).
26. Mangiarotti A, Chen N, Zhao Z, Lipowsky R, Dimova R. Membrane wetting, molding and reticulation by protein condensates. *bioRxiv*, 2022.2006.2003.494704 (2022).
27. Vorontsova I, *et al.* In vivo macromolecular crowding is differentially modulated by aquaporin 0 in zebrafish lens: Insights from a nanoenvironment sensor and spectral imaging. *Science Advances* **8**, eabj4833 (2022).

28. Thoke HS, *et al.* Tight Coupling of Metabolic Oscillations and Intracellular Water Dynamics in *Saccharomyces cerevisiae*. *PLOS ONE* **10**, e0117308 (2015).
29. Otaiza-González SaCMaRGaSRaMLaLRaBL. The innards of the cell: studies of water dipolar relaxation using the ACDAN fluorescent probe. *Methods and Applications in Fluorescence*, (2022).
30. Weber G, Farris FJ. Synthesis and spectral properties of a hydrophobic fluorescent probe: 6-propionyl-2-(dimethylamino)naphthalene. *Biochemistry* **18**, 3075-3078 (1979).
31. Gunther G, Malacrida L, Jameson DM, Gratton E, Sánchez SA. LAURDAN since Weber: The Quest for Visualizing Membrane Heterogeneity. *Accounts of Chemical Research* **54**, 976-987 (2021).
32. Thoke HS, Thorsteinsson S, Stock RP, Bagatolli LA, Olsen LF. The dynamics of intracellular water constrains glycolytic oscillations in *Saccharomyces cerevisiae*. *Scientific Reports* **7**, 16250 (2017).
33. Begarani F, *et al.* Capturing Metabolism-Dependent Solvent Dynamics in the Lumen of a Trafficking Lysosome. *ACS Nano* **13**, 1670-1682 (2019).
34. Bagatolli LA. LAURDAN Fluorescence Properties in Membranes: A Journey from the Fluorometer to the Microscope. In: *Fluorescent Methods to Study Biological Membranes* (eds Mély Y, Duportail G). Springer Berlin Heidelberg (2013).
35. Chen N, Zhao Z, Wang Y, Dimova R. Resolving the Mechanisms of Soy Glycinin Self-Coacervation and Hollow-Condensate Formation. *ACS Macro Letters* **9**, 1844-1852 (2020).
36. Chen N, Zhao M, Nicolai T, Chassenieux C. Exploiting Salt Induced Microphase Separation To Form Soy Protein Microcapsules or Microgels in Aqueous Solution. *Biomacromolecules* **18**, 2064-2072 (2017).
37. Ranjit S, Malacrida L, Jameson DM, Gratton E. Fit-free analysis of fluorescence lifetime imaging data using the phasor approach. *Nature Protocols* **13**, 1979-2004 (2018).
38. Malacrida L, Ranjit S, Jameson DM, Gratton E. The Phasor Plot: A Universal Circle to Advance Fluorescence Lifetime Analysis and Interpretation. *Annual Review of Biophysics* **50**, 575-593 (2021).
39. Adachi M, *et al.* Crystal structure of soybean 11S globulin: Glycinin A3B4 homohexamer. *Proceedings of the National Academy of Sciences* **100**, 7395-7400 (2003).
40. Brangwynne Clifford P, Tompa P, Pappu Rohit V. Polymer physics of intracellular phase transitions. *Nature Physics* **11**, 899-904 (2015).

41. Borchers W, Bremer A, Borgia MB, Mittag T. How do intrinsically disordered protein regions encode a driving force for liquid–liquid phase separation? *Current Opinion in Structural Biology* **67**, 41-50 (2021).
42. Uversky VN. Intrinsically disordered proteins in overcrowded milieu: Membrane-less organelles, phase separation, and intrinsic disorder. *Current Opinion in Structural Biology* **44**, 18-30 (2017).
43. Mangiarotti A, Bagatolli LA. Impact of macromolecular crowding on the mesomorphic behavior of lipid self-assemblies. *Biochimica et Biophysica Acta (BBA) - Biomembranes* **1863**, 183728 (2021).
44. Choe C, Lademann J, Darvin ME. Depth profiles of hydrogen bound water molecule types and their relation to lipid and protein interaction in the human stratum corneum in vivo. *Analyst* **141**, 6329-6337 (2016).
45. Đuričković I, Claverie R, Bourson P, Marchetti M, Chassot J-M, Fontana MD. Water–ice phase transition probed by Raman spectroscopy. *Journal of Raman Spectroscopy* **42**, 1408-1412 (2011).
46. Parasassi T, De Stasio G, Ravagnan G, Rusch RM, Gratton E. Quantitation of lipid phases in phospholipid vesicles by the generalized polarization of Laurdan fluorescence. *Biophysical Journal* **60**, 179-189 (1991).
47. Parasassi T, De Stasio G, d'Ubaldo A, Gratton E. Phase fluctuation in phospholipid membranes revealed by Laurdan fluorescence. *Biophysical Journal* **57**, 1179-1186 (1990).
48. Malacrida L, Astrada S, Briva A, Bollati-Fogolin M, Gratton E, Bagatolli LA. Spectral phasor analysis of LAURDAN fluorescence in live A549 lung cells to study the hydration and time evolution of intracellular lamellar body-like structures. *Biochimica et Biophysica Acta (BBA) - Biomembranes* **1858**, 2625-2635 (2016).
49. Leung SSW, Brewer J, Bagatolli LA, Thewalt JL. Measuring molecular order for lipid membrane phase studies: Linear relationship between Laurdan generalized polarization and deuterium NMR order parameter. *Biochimica et Biophysica Acta (BBA) - Biomembranes* **1861**, 183053 (2019).
50. Liu Y, Lipowsky R, Dimova R. Giant Vesicles Encapsulating Aqueous Two-Phase Systems: From Phase Diagrams to Membrane Shape Transformations. *Frontiers in Chemistry* **7**, 213 (2019).
51. Zhao Z, Roy D, Steinkühler J, Robinson T, Lipowsky R, Dimova R. Super-resolution imaging of highly curved membrane structures in giant vesicles encapsulating molecular condensates. *Advanced Materials* **34**, 2106633 (2021).

52. Liu Y, Agudo-Canalejo J, Grafmüller A, Dimova R, Lipowsky R. Patterns of Flexible Nanotubes Formed by Liquid-Ordered and Liquid-Disordered Membranes. *ACS Nano* **10**, 463-474 (2016).
53. Li Y, Kusumaatmaja H, Lipowsky R, Dimova R. Wetting-Induced Budding of Vesicles in Contact with Several Aqueous Phases. *The Journal of Physical Chemistry B* **116**, 1819-1823 (2012).
54. Golfetto O, Hinde E, Gratton E. Laurdan Fluorescence Lifetime Discriminates Cholesterol Content from Changes in Fluidity in Living Cell Membranes. *Biophysical Journal* **104**, 1238-1247 (2013).
55. Gratton E, Digman MA. Laurdan identifies different lipid membranes in eukaryotic cells. In: *Cell Membrane Nanodomains: from Biochemistry to Nanoscopy* (eds Cambi A, Lidke DS). CRC Press (2014).
56. Malacrida L, Jameson DM, Gratton E. A multidimensional phasor approach reveals LAURDAN photophysics in NIH-3T3 cell membranes. *Scientific Reports* **7**, 9215 (2017).
57. Liu Y, Lipowsky R, Dimova R. Concentration Dependence of the Interfacial Tension for Aqueous Two-Phase Polymer Solutions of Dextran and Polyethylene Glycol. *Langmuir* **28**, 3831-3839 (2012).
58. Botterbusch S, Baumgart T. Interactions between Phase-Separated Liquids and Membrane Surfaces. *Applied Sciences* **11**, (2021).
59. Gouveia B, Kim Y, Shaevitz JW, Petry S, Stone HA, Brangwynne CP. Capillary forces generated by biomolecular condensates. *Nature* **609**, 255-264 (2022).
60. Murakami K, Kajimoto S, Shibata D, Kuroi K, Fujii F, Nakabayashi T. Observation of liquid-liquid phase separation of ataxin-3 and quantitative evaluation of its concentration in a single droplet using Raman microscopy. *Chemical Science* **12**, 7411-7418 (2021).
61. Avni A, *et al.* Single-droplet vibrational raman spectroscopy illuminates the inner workings of phase-separated biomolecular condensates. *Biophysical Journal* **121**, 307a-308a (2022).
62. Alshareedah I, Kaur T, Banerjee PR. Chapter Six - Methods for characterizing the material properties of biomolecular condensates. In: *Methods in Enzymology* (ed Keating CD). Academic Press (2021).
63. Zimmermann T, Rietdorf J, Pepperkok R. Spectral imaging and its applications in live cell microscopy. *FEBS Letters* **546**, 87-92 (2003).
64. James NG, Ross JA, Štefl M, Jameson DM. Applications of phasor plots to in vitro protein studies. *Analytical Biochemistry* **410**, 70-76 (2011).

65. Dogra P, Joshi A, Majumdar A, Mukhopadhyay S. Intermolecular Charge-Transfer Modulates Liquid–Liquid Phase Separation and Liquid-to-Solid Maturation of an Intrinsically Disordered pH-Responsive Domain. *Journal of the American Chemical Society* **141**, 20380-20389 (2019).
66. Agarwal A, Arora L, Rai SK, Avni A, Mukhopadhyay S. Spatiotemporal modulations in heterotypic condensates of prion and α -synuclein control phase transitions and amyloid conversion. *Nature Communications* **13**, 1154 (2022).
67. Das D, Arora L, Mukhopadhyay S. Short-Range Backbone Dihedral Rotations Modulate Internal Friction in Intrinsically Disordered Proteins. *Journal of the American Chemical Society* **144**, 1739-1747 (2022).
68. Mitrea DM, Mittasch M, Gomes BF, Klein IA, Murcko MA. Modulating biomolecular condensates: a novel approach to drug discovery. *Nature Reviews Drug Discovery*, (2022).
69. Kilgore HR, Young RA. Learning the chemical grammar of biomolecular condensates. *Nature Chemical Biology*, (2022).
70. Chattopadhyay M, Krok E, Orlikowska H, Schwille P, Franquelim HG, Piatkowski L. Hydration Layer of Only a Few Molecules Controls Lipid Mobility in Biomimetic Membranes. *Journal of the American Chemical Society* **143**, 14551-14562 (2021).
71. Lee Y, Park S, Yuan F, Hayden CC, Choi SQ, Stachowiak JC. Lateral compression of lipids drives transbilayer coupling of liquid-like protein condensates. *bioRxiv*, 2022.2012.2021.521462 (2022).
72. Angelova MI, Soléau S, Méléard P, Faucon F, Bothorel P. Preparation of giant vesicles by external AC electric fields. Kinetics and applications. In: *Trends in Colloid and Interface Science VI* (eds Helm C, Lösche M, Möhwald H). Steinkopff (1992).
73. Kristoffersen AS, Erga SR, Hamre B, Frette Ø. Testing Fluorescence Lifetime Standards using Two-Photon Excitation and Time-Domain Instrumentation: Rhodamine B, Coumarin 6 and Lucifer Yellow. *Journal of Fluorescence* **24**, 1015-1024 (2014).
74. Malacrida L, Gratton E, Jameson DM. Model-free methods to study membrane environmental probes: a comparison of the spectral phasor and generalized polarization approaches. *Methods and Applications in Fluorescence* **3**, 047001 (2015).
75. Goormaghtigh E, Cabiaux V, Ruyschaert J-M. Secondary structure and dosage of soluble and membrane proteins by attenuated total reflection Fourier-transform infrared spectroscopy on hydrated films. *European Journal of Biochemistry* **193**, 409-420 (1990).